Author Manuscript

Author Manuscript

Author Manuscript

Author Manuscript

HHS Public Access

Author manuscript

Int J Radiat Biol. Author manuscript; available in PMC 2019 September 17.

Published in final edited form as:

Int J Radiat Biol. 2019 March ; 95(3): 338–346. doi:10.1080/09553002.2019.1554920.

MRI evaluation of the effects of whole brain radiotherapy on breast cancer brain metastasis

William Crowe[a], **Lulu Wang**[a], **Zhongwei Zhang**[a], **Jasmina Varagic**[b], **J. Daniel Bourland**[a,c], **Michael D. Chan**[c], **Amyn A. Habib**[d], **Dawen Zhao**[a,e]

[a]Department of Biomedical Engineering, Wake Forest School of Medicine, Winston-Salem, NC, USA;

[b]Department of Surgery, Wake Forest School of Medicine, Winston-Salem, NC, USA;

[c]Department of Radiation Oncology, Wake Forest School of Medicine, Winston-Salem, NC, USA;

[d]Department of Neurology and Neurotherapeutics, University of Texas Southwestern Medical Center and VA North Texas Medical Center, Dallas, TX, USA;

[e]Department of Cancer Biology, Wake Forest School of Medicine, Winston-Salem, NC, USA

Abstract

Purpose: To assess early changes in brain metastasis in response to whole brain radiotherapy (WBRT) by longitudinal Magnetic Resonance Imaging (MRI).

Materials and methods: Using a 7T system, MRI examinations of brain metastases in a breast cancer MDA-MD231-Br mouse model were conducted before and 24 hours after 3 daily fractionations of 4 Gy WBRT. Besides anatomic MRI, diffusion-weighted (DW) MRI and dynamic contrast-enhanced (DCE) MRI were applied to study cytotoxic effect and blood-tumor-barrier (BTB) permeability change, respectively.

CONTACT Dawen Zhao, dawzhao@wakehealth.edu, Department of Biomedical Engineering, Wake Forest School of Medicine, Medical Center Blvd, Winston-Salem, NC 27157, USA.

Notes on contributors

William Crowe is a Biomedical Engineering PhD candidate with particular research interests of MRI, breast cancer theranostics, and nano-delivery systems at Wake Forest School of Medicine.

Lulu Wang, MD, PhD is a Research Associate and laboratory manager with expertise in histology and cancer biology at the Wake Forest School of Medicine.

Zhongwei Zhang, MD, PhD is a Diagnostic Medical Physicist Resident with extensive MRI research experience in cancer models at Wake Forest School of Medicine.

Jasmina Veragic, MD, PhD is an Associate Professor with expertise in ultrasound applications and cardiology at Wake Forest School of Medicine.

Daniel Bourland, PhD is a Professor with expertise in radiation oncology and brain neoplasms at Wake Forest School of Medicine.

Michael Chan, MD is an Associate Professor with expertise in metastatic brain cancers and radiation therapy at Wake Forest School of Medicine.

Amyn Habib, MD is an Associate Professor with expertise in neurology and cancer biology at the University of Texas Southwestern Medical Center.

Dawen Zhao, MD, PhD is an Associate Professor with expertise in multimodal cancer imaging, cancer biology, and cancer nanotheranostics at Wake Forest School of Medicine.

Color versions of one or more of the figures in the article can be found online at www.tandfonline.com/irab

Disclosure statement

No potential conflict of interest was reported by the authors.

Author Manuscript Author Manuscript Author Manuscript Author Manuscript

Results: Before treatment, high-resolution T2-weighted images revealed hyperintense multifocal lesions, many of which (~50%) were not enhanced on T1-weighted contrast images, indicating intact BTB in the brain metastases. While no difference in the number of new lesions was observed, WBRT-treated tumors were significantly smaller than sham controls ($p < .05$). DW MRI detected significant increase in apparent diffusion coefficient (ADC) in WBRT tumors ($p < .05$), which correlated with elevated caspase 3 staining of apoptotic cells. Many lesions remained non-enhanced post WBRT. However, quantitative DCE MRI analysis showed significantly higher permeability parameter, K_{trans}, in WBRT than the sham group ($p < .05$), despite marked spatial heterogeneity.

Conclusions: MRI allowed non-invasive assessments of WBRT induced changes in BTB permeability, which may provide useful information for potential combination treatment.

Keywords

Brain metastasis; whole brain radiotherapy (WBRT); dynamic contrast-enhanced (DCE) MRI; diffusion-weighted (DW) MRI; blood-tumor-barrier (BTB); volume transfer coefficient Ktrans

Introduction

The incidence of brain metastasis from primary breast cancer has been increasing recently, with 5–15% of primary breast cancer patients now being diagnosed with brain metastasis at some point in their lives. In the case of triple negative and Her2+ breast cancers, incidence has increased to over 35% (Pestalozzi et al. 2006; Nayak et al. 2012). Increased breast cancer brain metastasis (BCBM) diagnosis is attributed to improved systemic therapies, an aging population, and increasingly frequent imaging (Wen 2001; Nayak et al. 2012). The prognosis for patients with these metastasis continues to be poor, with mean survival reported to be as low as 3.2 months (Niwinska et al. 2011).

The current standard of care for brain metastasis includes surgical resection, stereotactic radiosurgery (SRS) and/or whole brain radiotherapy (WBRT). Surgical resection, while useful on larger, solitary lesions, fails to improve patient outcome when multifocal lesions are present and is not useful for tumors in surgically inaccessible locations of the brain. SRS employs a single high dose of radiation to accurately target tumor lesions while minimizing damage to normal tissue. SRS is less invasive, and commonly applied to discrete metastasis, but may have limited use in treating multiple lesions (>4) (Soike et al. 2018). Whole Brain Radiotherapy (WBRT) has consistently been a standard of care treatment for multiple or numerous brain metastasis, designed to treat multiple lesions and occult micrometastases. WBRT is delivered to the entire brain in equally fractionated, daily treatments. WBRT has been shown to provide patients relief from neurologic symptoms, improve quality of life, and improve tumor control (Khuntia et al. 2006). However, deteriorating cognitive function has been frequently associated with WBRT. Nonetheless, with more patients than ever developing brain metastases, and survival time stagnantly short, there is an urgent need for a more effective treatment of brain metastatic disease.

Attempts to treat these metastatic lesions with traditional chemotherapeutics have been repeatedly stymied by the inability of traditional drugs to penetrate the blood-brain-barrier

Author Manuscript Author Manuscript Author Manuscript Author Manuscript

(BBB) in therapeutic concentrations, allowing the brain to exist as a ‘sanctuary site’ for metastases (Lockman et al. 2010). Indeed, extensive preclinical and clinical studies have demonstrated limited vascular permeability in brain metastases, in particular at their early stage of development. The traditional understanding of tumor vasculature and vascular permeability in brain metastases is largely based on invasive histological studies. These studies normally require many mice that are sacrificed at different time points after tumor implantation. More importantly, information about temporal development in individual lesions is absent from histological studies.

In vivo imaging promises greater efficiency since each animal serves as its own control and multiple time points can be sequentially examined. Because of its superb soft tissue contrast and spatial resolution, MRI is the most widely used imaging modality for brain tumors of human patients. We and others have applied small animal MRI to studying brain metastasis in rodent models. In our previous study, vascular permeability during intracranial tumor growth was investigated by longitudinal MRI in a mouse model of breast cancer MDA-MB231-Br (231-Br) brain metastasis (Zhou et al. 2013). Our data have demonstrated that a large percentage of brain metastases maintain intact BTB even at the late stage of disease, which is consistent with histological studies reported by others (Zhang et al. 1992; Lockman et al. 2010; Murrell et al. 2016).

Radiation has been implicated in increasing BBB/BTB permeability, which may enhance the accessibility of anti-cancer chemotherapeutics to tumor lesions in brain parenchyma. Given the nature of multifocal lesions in the intra-cardiac 231-Br brain metastasis model and the clinical utility of WBRT for brain metastases, in the current study, we applied longitudinal MRI to investigate the effects of WBRT on inhibition of tumor growth, new tumor development, tumor cell killing, and vascular permeability. A clinically relevant daily dose of 4 Gy was delivered to metastasis-bearing mouse brain for 3 consecutive days. While a 4 Gy × 5 dose schedule is used in the clinic (Rades et al. 2007), we aimed to determine if any changes, particularly in vascular permeability, occur at mid-WBRT, which may provide useful information for a potential combination with chemotherapeutics. In addition to high-resolution T2-w MRI for tumor detection and volume measurements, diffusion-weighted (DW) MRI and dynamic contrast-enhanced (DCE) MRI were conducted before and after 4 Gy × 3 WBRT to measure the parameters of apparent diffusion coefficient (ADC) and the volume transfer constant K_{trans}, respectively, for assessing tumor cell killing and changes in vascular permeability.

Materials and methods

Cell preparation

Human triple negative breast cancer MDA-MB-231-BR brain metastatic cell line (231-BR) was previously described (Yoneda et al. 2001; Palmieri et al. 2007; Zhou et al. 2013). The 231-BR cells (kindly provided by Dr. Steeg, NCI) were cultured in Dulbecco’s modified Eagle’s medium (DMEM) with 10% FBS, 1% L-Glutamine and 1% penicillin-streptomycin at 37°C with 5% CO_2. Once 80% confluence was achieved, the cells were harvested and suspended in serum-free medium.

Author Manuscript Author Manuscript Author Manuscript Author Manuscript

Breast cancer brain metastasis model

All animal procedures performed were approved by the Wake Forest University Institutional Animal Care and Use Committee. A total of 12 female nudes (BALB/c nu/nu) mice at 6–7 weeks old (Charles River Laboratories, Wilmington, MA) were used for this study. The intracardiac model of brain metastasis has been described previously (Zhou and Zhao 2014). In brief, mice were anesthetized with inhalation of isoflurane (3% induction, 1.5% maintenance). 2×10^5 231-BR cells in 50 μL of serum-free medium were injected directly into the left ventricle under imaging guidance of a small animal ultrasound (Vevo LAZR, FUJIFILM VisualSonics, Inc. Toronto, Canada).

Magnetic resonance imaging

MRI was performed on a 7T Bruker Biospin Small Animal scanner (Bruker Biospin, Rheinstetten, Germany) with a 30 cm diameter horizontal bore magnet and a maximum gradient strength of 200 mT/m. MRI was initiated 2 weeks after tumor cell injection and followed a week later to detect brain lesions. Animals were sedated with 3% isoflurane and maintained under general anesthesia (1.5% isoflurane). Animal body temperature and respiration were monitored and maintained constant throughout the experiment. A mouse tail vein was catheterized using a 27G butterfly for Gd-DTPA (Magnevist®; Bayer HealthCare, Wayne, NJ) contrast agent administration. Anatomical T2-W images, covering from the frontal lobe to the posterior fossa, were acquired using a Fast Spin Echo (FSE) sequence (TR/TE = 2500/50 ms; Echo Train Length (ETL): 8; Number of Scan Averages (NSA): 8; matrix size: 256 × 256; spatial resolution: 86 × 86 μm^2 in plane; scan time: 10 min 40 s). For assessing WBRT effects, immediately before and 24 h after the final dose of WBRT, a series of pulse sequences for T2-w, DW, DCE and T1-w post contrast MRI was performed sequentially. Diffusion-weighted MRI was acquired with single-shot echo planar imaging (EPI) using the following parameters: TR/TE = 2000/30 ms; *b*-values = 0, 500, and 1000 s/mm^2 equally in each of three orthogonal directions; matrix size: 128 × 128; NSA: 4; scan time: 11 min 44 s. Before DCE MRI, rapid high-resolution images for T1 mapping by variable flip angles was acquired (Brown et al. 2014). T1-w images were acquired using a FLASH sequence (TR/TE = 100/2.24 ms; FA = 5,10,20, and 35 degrees; NSA: 6; matrix size: 128 × 128; slices: 15; scan time per FA: 57 s). DCE-MRI was performed on 5 of the slices containing the most metastases using a FLASH T1-w sequence (TR/TE: 43/2.3; FA: 30 degrees; matrix size: 128 × 128: NSA: 2; scan time per acquisition: 8 s). Fifty dynamic images over 7 mins were collected before and after manual i.v. bolus injection of Gd-DTPA (0.1 mmol/kg). Finally, T1-w contrast-enhanced images were acquired with a FSE sequence (TR/TE: 800/7 ms; ETL: 4; NSA: 8; matrix size: 256 × 256; spatial resolution 86 × 86 μm; scan time 5 min 7 s).

Whole brain radiation therapy

Multifocal brain metastases were confirmed in all 12 mice by MRI. However, one animal was found to have an unusually high number of tumor lesions and thus was removed from the study after confirmation by outlier analysis. Once brain metastasis was confirmed by MRI, the tumor-bearing mice were randomly assigned to either WBRT ($n = 6$) or sham ($n = 5$) treatment group. The mice were anesthetized with inhaled 3% isoflurane and each mouse

Author Manuscript Author Manuscript Author Manuscript Author Manuscript

of the WBRT group ($n = 6$) received a total of 12 Gy in 3 daily doses of 4 Gy (4 Gy × 3). Radiation was delivered using an X-RAD 320 orthovoltage irradiator (Precision X-ray, North Branford, CT) at 300 kV, 1 mm Pb HVL, at a dose rate of 233 cGy/min. Each animal was carefully positioned supine under a rectangular Lipowitz alloy collimator of 10 × 15 mm for each fraction of radiation, aligning the collimator field edges with landmarks of the skull and avoiding eye regions.

Data analysis

General image analysis—All imaging analysis was conducted using house-made MATLAB scripts (Mathworks, Natick, MA). Prior to quantitative mapping and analysis, 3-by-3 median filtering was conducted on all raw images to reduce noise. All images were co-registered and upsized to the dimensions of T2-w images for analysis. Tumor volumes were estimated from T2-w images by manually outlining the enhancing portion of the mass on each image, excluding any hyperintense CSF or edema. Semi-automated thresholding and histogram analysis were conducted on the outline to precisely define tumor tissue. T1-CE image analysis was conducted by comparing contrast-enhanced T1-w images to T1-w images without contrast to define regions with contrast enhancement.

T1 mapping—T1 values were computed from collected multiple flip angle T1-w images by voxel-wise data fitting to Equation (1):

$$S_i = S_0 * \sin(\alpha) \frac{\left(1 - \exp\left[\frac{-T_R}{T_1}\right]\right)}{\left(1 - \exp\left[\frac{-T_R}{T_1}\right]\cos(\alpha)\right)} \quad (1)$$

Where S_i is the signal intensity at a given flip angle (α), S_0 is the raw voxel intensity, and T_R is the repetition time. Here the assumption is made that $T_E < T_2^*$ (Eminian et al. 2018).

DW MRI—ADC mapping was accomplished by conducting voxel-wise fitting of DW image signal intensities to the Stejskal-Tanner equation (Equation 2) using a least-squares approach (Sener 2001; Westin et al. 2002).

$$S(b) = S_0 e^{-b(ADC)} \quad (2)$$

Where $S(b)$ is the signal intensity at a non-zero b-value, S_0 is the signal intensity without diffusion gradients, b is the diffusion weighting factor (Li et al. 2007; Yankeelov et al. 2007). Voxels where fitting did not converge to physiologically relevant values were excluded from analysis (those with ADC ≥ 3.0×10^{-3} mm^2/s indicating free water at body temperature or ≤0 mm^2/s indicating no diffusion). Changes in ADC values were calculated by averaging voxel ADC values on a tumor-wise basis. All lesions with physiologically relevant ADC and good curve fitting were included in the analysis.

Author Manuscript Author Manuscript Author Manuscript Author Manuscript

DCE MRI—A series of T1-w images was continuously acquired pre and post manual i.v. bolus injection of Gd-DTPA (0.1 mmol/kg) via the tail vein. DCE MRI data were modeled to permeability K_{trans} maps using the generalized kinetic model (GKM). Previous studies have validated the GKM model in murine BBB opening (Zhou et al. 2004; Egeland et al. 2006; Luypaert et al. 2011; Vlachos et al. 2011) as a two-compartment model with blood plasma and extravascular extracellular space (EES) compartments (Tofts 2010).

$$\frac{dC_t}{dt} = K_{trans}C_p - k_{ep}C_t \quad (3)$$

Where K_{trans} is the transfer rate constant from the blood plasma into the EES, K_{ep} is the transfer rate from the EES to the blood plasma, C_p is the concentration of Gd-DTPA in the blood plasma, and C_t is the concentration of Gd-DTPA in the EES. C_p determines the AIF through fitting with the bi-exponential equation:

$$C_p(t) = \sum_{n=1}^{2} A_n e^{-K_n t} \quad (4)$$

Where A_n represents the n^{th}-pass peak amplitude of C_p, K_n represents the decay rate constant of C_p for pass n, and t is time. Direct AIF quantification is difficult in many models, particularly small animal models, necessitating AIF estimation (McGrath et al. 2009). T1-w image signal intensity is transformed to contrast agent concentration using the Soloman-Bloembergen equation, as previously described (Buonaccorsi et al. 2005; Vlachos et al. 2011).

$$[Gd] = \frac{S_i - S_0}{T_{1.pre} * r_1 * S_0} \quad (5)$$

Where S_0 and S_i are the voxel signal intensities before and after contrast administration, respectively, $T_{1.pre}$ is the longitudinal relaxation time of tissue before contrast administration, r_1 is the longitudinal relaxivity of the contrast agent (r_1 = 3:1 $s^{-1}mM^{-1}$ for Gd-DTPA at 7T) (Shen et al. 2015).

The nature of this study emphasizes K_{trans}, although the GKM considers both K_{trans} and K_{ep}, K_{ep} as a variable determines the curve shape or ‘steady state’ considerations, while K_{trans} primarily impacts the curve amplitude and changes directly after contrast is applied (Tofts 2010; Vlachos et al. 2011).

Immunohistochemistry

Animals were sacrificed promptly after the last MRI scan; brains (n = 3 from each group) were dissected and fixed in 4% paraformaldehyde (PFA). The frozen OCT embedded whole brains were cryosectioned (10 μm). Apoptosis staining was conducted using anti-caspase-3 antibody (1:300; Cell Signaling, Danvers, MA) followed by secondary HRP- conjugated

Author Manuscript Author Manuscript Author Manuscript Author Manuscript

goat anti-rabbit secondary antibody (1:1000; Jackson Immunoresearch Laboratory, West Grove, PA). Tumor regions and their surrounding normal brains were examined under a microscope for positive staining. Percentage of apoptotic tumor cells was determined by counting the number of Caspase 3-positive cells relative to the total number of tumor cells (Zhao et al. 2005).

Statistical analysis

Statistical analysis was conducted using MATLAB (Mathworks, Natick, MA). Statistical significance was determined by using unpaired *t*-tests to compare pre- and post-treatment data both within and across the groups for Tumor Volume, ADC, and DCE MRI derived parameters. $p < .05$ was considered to indicate statistical significance.

Results

Ultrasound image-guided left ventricular injection of 231-BR cells ensured successful development of brain metastasis in all 12 nude mice. In concurrence with our previous study of the 231-Br, longitudinal MRI started to visualize hyperintense brain metastases on T2-w images 3 weeks post-injection. These brain metastases distributed widely across the mouse brain. Prior to treatment, T2-w MRI revealed a total of 89 individual lesions in the WBRT mice ($n = 6$), while a total of 101 lesions in the sham irradiation group ($n = 5$) (Figure 1(a)). Tumor size ranged from 0.06 mm^3 to 0.53 mm^3 in the WBRT group (mean = 0.23 ± 0.12 mm^3), and from 0.06 mm^3 to 1.85 mm^3 in the sham group (mean = 0.28 ± 0.22 mm^3; Figure 1(b)). One day after completion of the 3 daily doses of 4 Gy, follow-up MRI detected an increase in the number of lesions in each group ($n = 116$ for WBRT; $n = 140$ for sham), indicating the development of new metastases (Figure 1(b,c)). Compared to the pre-treatment, post-treatment tumor size was found to become significantly larger in both of the groups ($p < .01$; Figure 1). However, mean tumor size post-treatment was 0.34 ± 0.21 mm^3 for the WBRT group, significantly smaller than that of the sham group (mean = 0.44 ± 0.31 mm^3, $p < .01$; Figure 1(b) and Table 1). Although 42% more new lesions were observed at the follow-up scans in the sham group, compared to a 21% increase in the WBRT, there was no significant difference found between the two groups (Figure 1(c)).

Tumor ADC maps were generated from DW MRI based on 3 *b* values of 0, 500, and 1000. As described in Methods, those tumor lesions that did not have reliable curve-fitting of ADC were excluded from the analysis. As a result, the WBRT mice ($n = 6$) had a total of 44 and 65 individual lesions for pre and post-treatment ADC analysis, respectively; the sham-irradiated mice ($n = 5$) contained 59 pre and 90 post-treatment ADC maps. The contralateral healthy brain as reference tissues was assessed for changes in ADC, but no inter or intra-group difference was observed (Table 1). As shown in Figure 2(a), ADC maps revealed inter and intratumoral heterogeneity in both pre- and post-treated tumors. The histogram plots of the voxel by voxel ADC values of individual lesions all showed a right-shift after WBRT, indicating an increase in ADC at post-treatment. The sham irradiated tumors also showed a tendency of a shift towards the right, but seemed more subtle (Figure 2). For WBRT tumors, mean ADC at pre-treatment was $0.75 \pm 0.01 \times 10^{-3}$ mm^2/s, which increased significantly after WBRT ($0.83 \pm 0.02 \times 10^{-3}$ mm^2/s; $p < .01$; Figure 2(b) and Table 1). There was no

Author Manuscript Author Manuscript Author Manuscript Author Manuscript

significant change in ADC found between pre and post-sham irradiated tumors (0.75 ± 0.01 vs. 0.77 ± 0.02 × 10^{-3} mm^2/s; Figure 2(b)). Moreover, the post-WBRT tumors had a significantly higher ADC compared to the sham tumors ($p < .01$, Figure 2(b)). A correlative immunohistochemical study with anti-caspase antibody showed that the WBRT tumors had significantly more apoptotic tumor cells than the sham-irradiated tumors (mean = 8.2 ± 0.8% vs. 3.0 ± 0.3%; $p < .05$; Figure 3).

BTB permeability of brain metastases was investigated by two approaches: T1-w contrast-enhanced images and quantitative K_{trans} maps derived from DCE MRI. At pre- and post-treatment, T1-w contrast-enhanced images were acquired 7 mins after manual i.v. bolus injection of Gd-DTPA, respectively. Out of a total of 190 lesions from the pre-treated WBRT and sham groups, 90 lesions (47%) were enhanced (46 ± 8% and 49 ± 8% for WBRT and sham, respectively; Figure 4 and Table 1). The result was in a good agreement with our previous study of the 231-BR brain metastases, reiterating that a large fraction of brain metastases keep intact BTB. The number of enhanced lesions increased significantly at post-treatment in both of the WBRT (71 ± 4%; $p < .05$) and sham (62 ± 5%; $p < .05$) group; however, there was no significant difference between the two groups (Figure 4).

The K_{trans} permeability map generated from DCE MRI was used to assess the degree of BTB disruption. As shown in Figure 5, the K_{trans} maps based on voxel by voxel analysis clearly showed not only intertumoral variation but also intratumoral heterogeneity in vascular permeability. Quantitative K_{trans} data were presented in histogram plots (Figure 5(a)). Compared to pre-treatment, post-treatment K_{trans} increased in both the WBRT (mean = 0.048 ± 0.005 vs.0.073 ± 0.007 min^{-1}) and sham irradiated tumors (mean = 0.050 ± 0.005 vs. 0.056 ± 0.003 min^{-1}; Figure 5(a,b) and Table 1). Statistical comparisons found significantly increased K_{trans} only in the WBRT group ($p < .05$). Moreover, post-treatment WBRT tumors had a significantly higher K_{trans} than the sham-irradiated tumors ($p < .05$; Figure 5(b)). Contralateral healthy brain as reference tissues were assessed for changes in K_{trans}, but no inter or intra-group difference was observed.

Discussion

In the present study, we applied longitudinal high-resolution MRI to evaluate the early effects of clinically relevant WBRT on metastatic tumor burden, tumor cell killing and BBB/BTB permeability in a murine BCBM model. In good agreement with our previous study of this 231-Br BCBM model (Zhou et al. 2013), high-resolution T2-W images revealed hyperintense multifocal tumor lesions with a minimum diameter of 172 μm, ~50% of which did not show enhancement on T1-w post contrast images (Figure 2 and Table 1), indicating that many brain metastases retain intact BTB. WBRT with a hyperfractionation scheme of 4 Gy × 5 is applied clinically for brain metastasis treatment. However, the goal of this work was not to study the effects of a complete course of WBRT, but rather to investigate early effects occurring at mid-WBRT, for the purpose of defining a ‘therapeutic window’ which may be useful for synergistic application of either traditional or novel chemotherapeutics. Moreover, hyperfractionated WBRT has been considered as a likely cause of clinical cognitive decline in brain metastasis patients. Thus, if fractionations were reduced, WBRT induced cognitive complications may be alleviated.

Author Manuscript Author Manuscript Author Manuscript Author Manuscript

As soon as 24 hours after completion of the daily 4 Gy WBRT over 3 days, the follow-up MRI was conducted and T2-w MRI showed significantly delayed tumor growth in the WBRT tumors, as compared to the sham controls (Figure 1 and Table 1). However, the WBRT was not shown to inhibit the development of new lesions. These results are in line with previously published data of BCBM despite the total doses and fractionations of WBRT that varied in these studies (Smart et al. 2015; Murrell et al. 2016). Murrell and colleagues applied a higher dose WBRT of 20 Gy in 2 fractions to a mouse model of MDA-MB231-Br-Her2, a genetically modified 231-Br overexpressing Her-2. For a prolonged period of MRI follow-up up to 12 days post WBRT, mean tumor volume, but not the number of lesions, was found to decrease significantly in the WBRT group (Murrell et al. 2016). In another recent study by Smart and colleagues aiming to compare a single high dose with fractionated WBRT, the clinically relevant 3 Gy × 10 was found to be superior to a single 15 Gy WBRT in terms of tumor growth inhibition of both macrometastases and micrometastases in the 231-Br mouse model (Smart et al. 2015).

Concurring with anatomic MRI of tumor growth delay induced by WBRT, DW MRI detected significantly increased ADC in the WBRT tumors (Figure 2). DW MRI by measuring the microscopic mobility of water can provide information about the cellular structure, i.e. cell density (Hamstra et al. 2007; Padhani et al. 2009; Zhao et al. 2011). ADC that is extracted from DW images with multiple b values has been reported to correlate inversely with cell density, in which lower ADC values indicate higher cellularity, whereas treatment induced apoptosis and/or necrotic tissue show high ADC (Zhao et al. 2011). The cytotoxic effect of WBRT was further supported by immunohistochemical studies, showing significantly higher caspase 3 staining in the WBRT treated brain metastases (Figure 3).

It has been well documented that ionizing radiation induces BBB disruption in a dose and time-dependent manner (Li et al. 2003; Yuan et al. 2006; Sandor et al. 2014). However, few studies have investigated the effect of clinically relevant WBRT fractionation schemes on BBB/BTB permeability in brain metastasis models. On the contrary, a single higher dose of WBRT has been commonly involved in such studies. In the present study, we adopted a clinical dose schedule with a daily 4 Gy WBRT to treat brain metastases, aiming to determine if BTB permeability is affected at the middle of the 4 Gy × 5 WBRT when the first 3 doses were completed. T1-w contrast-enhanced images acquired after i.v. bolus injection of Gd-DTPA has widely been used to interrogate BBB permeability. In a good agreement with our previous study of the 231-Br brain metastases (Zhou et al. 2013), a high fraction of brain metastases remains impermeable to Gd-DTPA. Despite the increased number of lesions that were enhanced in the post-treatment MRI, WBRT did not increase the BTB permeability compared to the sham controls (Figure 4). These observations also coincided with the study reported by Murrell et al (Murrell et al. 2016), reiterating the heterogeneous nature of BTB permeability among individual lesions.

In addition to T1-w contrast-enhanced imaging, quantitative MRI methods are increasingly common in preclinical BBB permeability assessment. Tofts model is a quantitative two-compartment pharmacokinetic model of tissue permeability and has become the standard in dynamic contrast-enhanced (DCE) MRI (Tofts et al. 1995). The Tofts model relies on serial rapid T1-w imaging over the course of a systemic Gd-DTPA administration, providing a

Author Manuscript Author Manuscript Author Manuscript Author Manuscript

measurement of T1-w signal enhancement as a function of time. These images are fitted voxel-wise to the model described in Equation 3 to formulate a quantitative map of tissue permeability. An arterial input function (AIF), required by this model, is formulated by the bi-exponential model found in Equation 4, which has been used for previous research and found to be an accurate approximation of the AIF in small animal models (Pickup et al. 2003; McGrath et al. 2009).

K_{trans}, which has been generally used as a measure of vascular permeability, was extracted from DCE MRI; K_{trans} maps of individual lesions were generated to provide voxel by voxel measurement of intratumoral permeability. As expected, K_{trans} maps clearly revealed marked inter- and intra-tumoral heterogeneity in BTB permeability (Figure 5). Intriguingly, in contrast to the data of T1-w post-contrast images, showing no difference in BTB permeability between the WBRT tumors and the sham controls (Figure 4), quantitative DCE analysis detected a significant increase in mean K_{trans} of the WBRT tumors observed at post-treatment (Figure 5). Gd-DTPA, a small molecule MRI contrast agent, has a molecular weight similar to that of many chemotherapeutic agents, e.g. doxorubicin and paclitaxel, or some small molecule tyrosine kinase inhibitor such as lapatinib. Thus, one may reason that the WBRT enhanced BTB permeability to Gd-DTPA is also applicable to the abovementioned small molecules of therapeutic agents. However, it is noteworthy that other chemicophysical properties, e.g. electric charge and lipophilicity, also contribute significantly to their BBB permeability. Moreover, Lockman and colleagues assessed the uptake of radio-labeled paclitaxel or doxorubicin in brain metastases of the 231-Br-Her2 mouse model. Their data showed that the drug concentrations even in those permeable metastases were far below that in visceral metastases (Lockman et al. 2010). Along with our observations in the prior and current studies, these results supported the notion that the BTB of brain metastases are remarkably heterogeneous, which may prevent therapeutic doses of anti-cancer drugs penetrating and distributing homogeneously across the tumors. Nevertheless, to the best of our knowledge, the current study is the first one to apply MRI to analyzing the quantitative change in BTB permeability of brain metastases in response to a clinically relevant WBRT dose schedule.

In the present study, we have applied longitudinal MRI to evaluate the early effects of WBRT on BCBM. In addition to anatomic MRI, multimodal functional MRI approaches provided quantitative analysis of temporal and spatial changes in both tumor tissue and vasculature in response to WBRT, of which the information about BTB permeability change may be particularly useful for possible combination treatment with systemic chemotherapeutic agents.

Acknowledgements

We are grateful to Drs. Diane Palmieri and Patricia Steeg (CCR, NCI) for providing breast cancer MDA-MB231-Br cells. We are also grateful to Dr. Youngkyoo Jung for his assistance and technical support.

Funding

This research has been supported in part by the Department of Defense Breast Cancer Idea Award [Grant number W81XWH-12-1-0317]; National Institute of Health/National Cancer Institute [Grant number R01CA194578]; Wake Forest Comprehensive Cancer Center [Grant number P30 CA01219740] and the Wells Fargo Scholar Program; AH is supported by a Merit Award from the Department of Veteran's Affairs.

Author Manuscript Author Manuscript Author Manuscript Author Manuscript

References

Brown RW, Haacke EM, Cheng Y-CN, Thompson MR, Venkatesan R. 2014 Magnetic resonance imaging: physical principles and sequence design. John Wiley & Sons Hoboken, New Jersey.

Buonaccorsi GA, Roberts C, Cheung S, Watson Y, Davies K, Jackson A, Jayson GC, Parker GJ. 2005 Tracer kinetic model-driven registration for dynamic contrast enhanced MRI time series. Med Image Comput Comput Assist Interv. 8:91–98. [PubMed: 16685833]

Egeland TA, Gaustad JV, Vestvik IK, Benjaminsen IC, Mathiesen B, Rofstad EK. 2006 Assessment of fraction of radiobiologically hypoxic cells in human melanoma xenografts by dynamic contrast-enhanced MRI. Magn Reson Med. 55:874–882. [PubMed: 16506163]

Eminian S, Hajdu SD, Meuli RA, Maeder P, Hagmann P. 2018 Rapid high resolution T1 mapping as a marker of brain development: normative ranges in key regions of interest. PLoS One. 13:e0198250. [PubMed: 29902203]

Hamstra DA, Rehemtulla A, Ross BD. 2007 Diffusion magnetic resonance imaging: a biomarker for treatment response in oncology. J Clin Oncol. 25:4104–4109. eng. [PubMed: 17827460]

Khuntia D, Brown P, Li J, Mehta MP. 2006 Whole-brain radiotherapy in the management of brain metastasis. J Clin Oncol. 24:1295–1304. [PubMed: 16525185]

Li J, Bentzen SM, Renschler M, Mehta MP. 2007 Regression after whole-brain radiation therapy for brain metastases correlates with survival and improved neurocognitive function. J Clin Oncol. 25: 1260–1266. [PubMed: 17401015]

Li YQ, Chen P, Haimovitz-Friedman A, Reilly RM, Wong CS. 2003 Endothelial apoptosis initiates acute blood-brain barrier disruption after ionizing radiation. Cancer Res. 63:5950–5956. [PubMed: 14522921]

Lockman PR, Mittapalli RK, Taskar KS, Rudraraju V, Gril B, Bohn KA, Adkins CE, Roberts A, Thorsheim HR, Gaasch JA. 2010 Heterogeneous blood-tumor barrier permeability determines drug efficacy in experimental brain metastases of breast cancer. Clin Cancer Res. 16:5664–5678. eng. [PubMed: 20829328]

Luypaert R, Sourbron S, de Mey J. 2011 Validity of perfusion parameters obtained using the modified Tofts model: a simulation study. Magn Reson Med. 65:1491–1497. [PubMed: 21500273]

McGrath DM, Bradley DP, Tessier JL, Lacey T, Taylor CJ, Parker GJ. 2009 Comparison of model-based arterial input functions for dynamic contrast-enhanced MRI in tumor bearing rats. Magn Reson Med. 61: 1173–1184. [PubMed: 19253360]

Murrell DH, Zarghami N, Jensen MD, Chambers AF, Wong E, Foster PJ. 2016 Evaluating changes to blood-brain barrier integrity in brain metastasis over time and after radiation treatment. Transl Oncol. 9: 219–227. [PubMed: 27267840]

Nayak L, Lee EQ, Wen PY. 2012 Epidemiology of brain metastases.Curr Oncol Rep. 14:48–54. [PubMed: 22012633]

Niwińska A, Olszewski W, Murawska M, Pogoda K. 2011 Triple-negative breast cancer with brain metastases: a comparison between basal-like and non-basal-like biological subtypes. J Neurooncol. 105: 547–553. [PubMed: 21656328]

Padhani AR, Liu G, Mu-Koh D, Chenevert TL, Thoeny HC, Takahara T, Dzik-Jurasz A, Ross BD, Van Cauteren M, Collins D, et al. 2009 Diffusion-weighted magnetic resonance imaging as a cancer bio-marker: consensus and recommendations. Neoplasia. 11:102–125. eng. [PubMed: 19186405]

Palmieri D, Bronder JL, Herring JM, Yoneda T, Weil RJ, Stark AM, Kurek R, Vega-Valle E, Feigenbaum L, Halverson D, et al. 2007 Her-2 overexpression increases the metastatic outgrowth of breast cancer cells in the brain. Cancer Res. 67:4190–4198. eng. [PubMed: 17483330]

Pestalozzi BC, Zahrieh D, Price KN, Holmberg SB, Lindtner J, Collins J, Crivellari D, Fey MF, Murray E, Pagani O, et al. 2006 Identifying breast cancer patients at risk for Central Nervous System (CNS) metastases in trials of the International Breast Cancer Study Group (IBCSG). Ann Oncol. 17:935–944. [PubMed: 16603601]

Pickup S, Zhou R, Glickson J. 2003 MRI estimation of the arterial input function in mice. Acad Radiol. 10:963–968. [PubMed: 13678084]

Author Manuscript Author Manuscript Author Manuscript Author Manuscript

Rades D, Bohlen G, Lohynska R, Veninga T, Stalpers LJ, Schild SE, Dunst J, et al. 2007 Whole-brain radiotherapy with 20 Gy in 5 fractions for brain metastases in patients with cancer of unknown primary (CUP). Strahlenther Onkol. 183:631–636. eng. [PubMed: 17960339]

Sandor N, Walter FR, Bocsik A, Santha P, Schilling-Toth B, Lener V, Varga Z, Kahan Z, Deli MA, Safrany G, et al. 2014 Low dose cranial irradiation-induced cerebrovascular damage is reversible in mice. PLoS One. 9:e112397 eng. [PubMed: 25393626]

Sener RN. 2001 Diffusion MRI: apparent diffusion coefficient (ADC) values in the normal brain and a classification of brain disorders based on ADC values. Comput Med Imaging Graph. 25:299–326. [PubMed: 11356324]

Shen Y, Goerner FL, Snyder C, Morelli JN, Hao D, Hu D, Li X, Runge VM. 2015 T1 relaxivities of gadolinium-based magnetic resonance contrast agents in human whole blood at 1.5, 3, and 7 T. Invest Radiol. 50:330–338. [PubMed: 25658049]

Smart D, Garcia-Glaessner A, Palmieri D, Wong-Goodrich SJ, Kramp T, Gril B, Shukla S, Lyle T, Hua E, Cameron HA, et al. 2015 Analysis of radiation therapy in a model of triple-negative breast cancer brain metastasis. Clin Exp Metastasis. 32:717–727. eng. [PubMed: 26319493]

Soike MH, Hughes RT, Farris M, McTyre ER, Cramer CK, Bourland JD, Chan MD. 2018 Does stereotactic radiosurgery have a role in the management of patients presenting with 4 or more brain meta-stases?. Neurosurgery. nyy216.

Tofts PS. 2010 T1-weighted DCE imaging concepts: modelling, acquisition and analysis. Signal. 500:400.

Tofts PS, Berkowitz B, Schnall MD. 1995 Quantitative analysis of dynamic Gd-DTPA enhancement in breast tumors using a permeability model. Magn Reson Med. 33:564–568. [PubMed: 7776889]

Vlachos F, Tung YS, Konofagou E. 2011 Permeability dependence study of the focused ultrasound-induced blood-brain barrier opening at distinct pressures and microbubble diameters using DCE-MRI. Magn Reson Med. 66:821–830. [PubMed: 21465543]

Wen PY. 2001 Metastatic brain cancer Cancer: principles and practice of oncology. 6th ed. Lippincott Williams & Wilkins Philadelphia, PA

Westin CF, Maier SE, Mamata H, Nabavi A, Jolesz FA, Kikinis R. 2002 Processing and visualization for diffusion tensor MRI. Med Image Anal. 6:93–108. [PubMed: 12044998]

Yankeelov TE, Lepage M, Chakravarthy A, Broome EE, Niermann KJ, Kelley MC, Meszoely I, Mayer IA, Herman CR, McManus K, et al. 2007 Integration of quantitative DCE-MRI and ADC mapping to monitor treatment response in human breast cancer: initial results. Magn Reson Imaging. 25:1–13. [PubMed: 17222711]

Yoneda T, Williams PJ, Hiraga T, Niewolna M, Nishimura R. 2001 A bone-seeking clone exhibits different biological properties from the MDA-MB-231 parental human breast cancer cells and a brain-seeking clone in vivo and in vitro. J Bone Miner Res. 16:1486–1495. [PubMed: 11499871]

Yuan H, Gaber MW, Boyd K, Wilson CM, Kiani MF, Merchant TE. 2006 Effects of fractionated radiation on the brain vasculature in a murine model: blood-brain barrier permeability, astrocyte proliferation, and ultrastructural changes. Int J Radiat Oncol Biol Phys. 66: 860–866. eng. [PubMed: 17011458]

Zhang RD, Price JE, Fujimaki T, Bucana CD, Fidler IJ. 1992 Differential permeability of the blood-brain barrier in experimental brain metastases produced by human neoplasms implanted into nude mice. Am J Pathol. 141:1115–1124. eng. [PubMed: 1443046]

Zhao D, Chang CH, Kim JG, Liu H, Mason RP. 2011 In vivo near-infrared spectroscopy and magnetic resonance imaging monitoring of tumor response to combretastatin A-4-phosphate correlated with therapeutic outcome. Int J Radiat Oncol Biol Phys. 80:574–581. eng. [PubMed: 21345614]

Zhao D, Jiang L, Hahn EW, Mason RP. 2005 Continuous low-dose (metronomic) chemotherapy on rat prostate tumors evaluated using MRI in vivo and comparison with histology. Neoplasia. 7:678–687. [PubMed: 16026647]

Zhou H, Chen M, Zhao D. 2013 Longitudinal MRI evaluation of intracranial development and vascular characteristics of breast cancer brain metastases in a mouse model. PLoS One. 8: e62238. [PubMed: 23638013]

Zhou H, Zhao D. 2014 Ultrasound imaging-guided intracardiac injection to develop a mouse model of breast cancer brain metastases followed by longitudinal MRI. J Vis Exp. (85):51146

Author Manuscript Author Manuscript Author Manuscript Author Manuscript

Zhou R, Pickup S, Yankeelov TE, Springer CS Jr, Glickson JD. 2004 Simultaneous measurement of arterial input function and tumor pharmacokinetics in mice by dynamic contrast enhanced imaging: effects of transcytolemmal water exchange. Magn Reson Med. 52: 248–257. [PubMed: 15282806]

Author Manuscript Author Manuscript Author Manuscript Author Manuscript

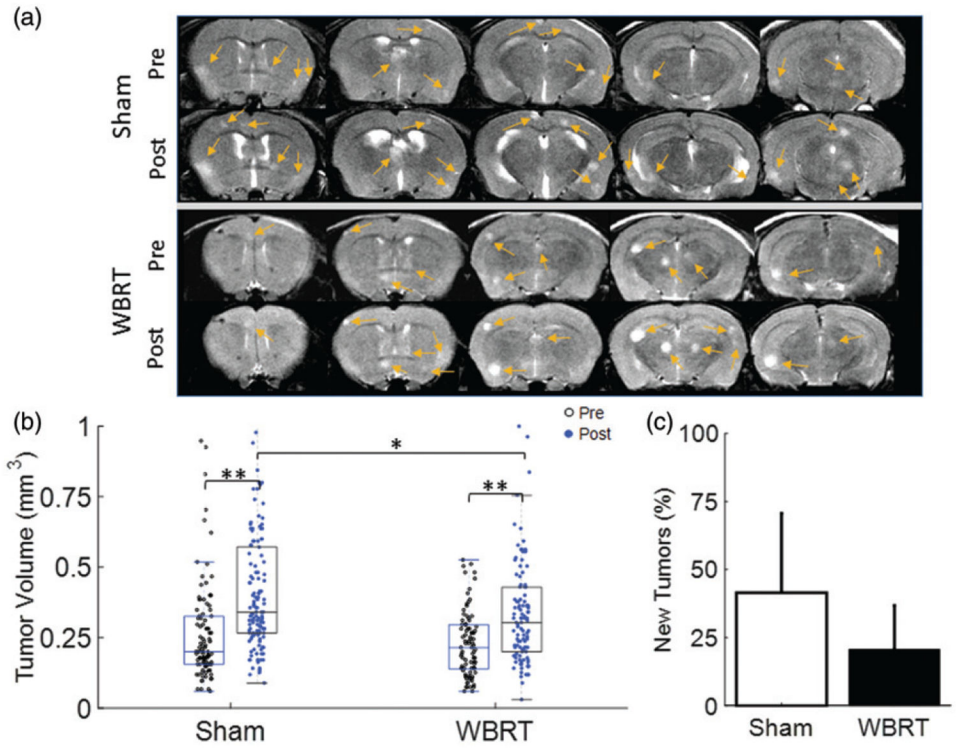

Figure 1.

Tumor burden in response to WBRT. (a) T2-w images of a representative WBRT and Sham-treated mouse brain were acquired at pre and post-treatment, respectively. Five consecutive axial MRI sections revealed multifocal hyperintense lesions (arrows) in brains of both groups. (b) Tumor volume of individual brain metastases at pre (empty dot) versus post (solid dot) treatment was plotted. Significant increase in tumor volume at post-treatment was observed in each group: for the sham group, mean tumor volume = 0.28 ± 0.22 (n = 101) at pre increased to 0.44 ± 0.31 (n = 140; p < .01); for the WBRT, mean tumor volume = 0.23 ± 0.12 mm^3 (n = 89) at pre increased to 0.34 ± 0.21 mm^3 (n = 116; p < .01)). At post-treatment, the sham-treated tumors were found to be significantly larger than the WBRT tumors (p < .05). (c) An incidence of new tumor development at post-treatment was also studied. There was a 42 ± 29% increase in the number of brain lesions in the sham group, while a smaller increase (21 ± 16%) was found in the WBRT group. However, there was no significant difference between the groups. Mean ± SD, *p < .05, **p < .01.

Author Manuscript Author Manuscript Author Manuscript Author Manuscript

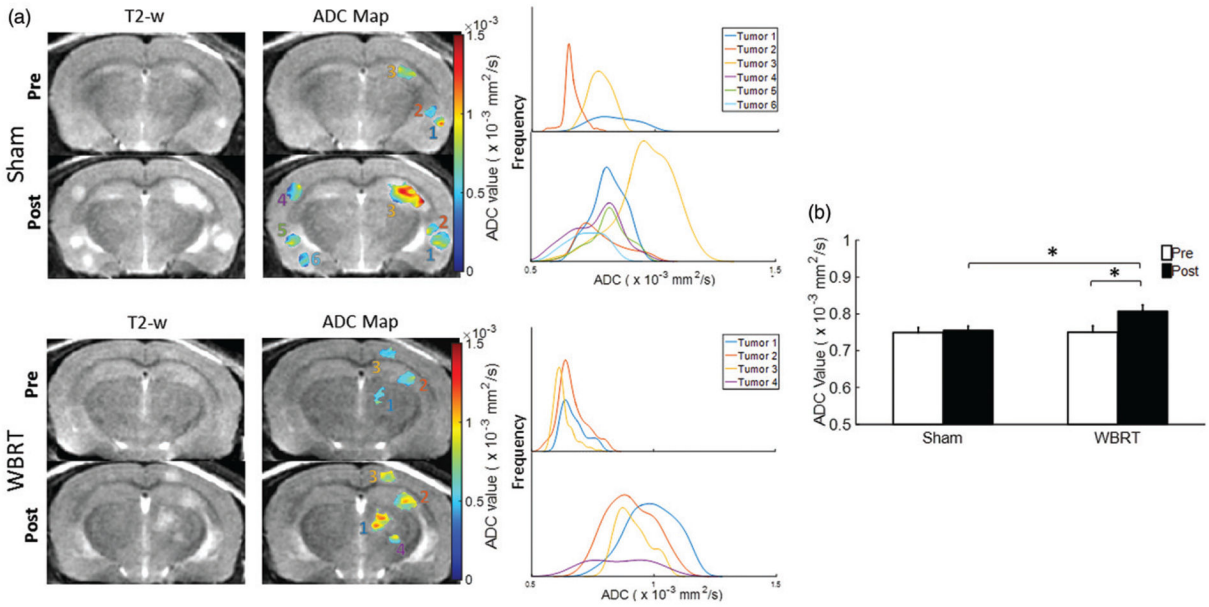

Figure 2.

Diffusion-weighted MRI evaluating tumor response to WBRT. (a) DW MRI was conducted at pre and post-treatment on both the sham and WBRT treated mouse brains. Representative ADC maps of individual lesions were generated and overlaid on T2-w images. Corresponding histograms of voxel-by-voxel ADC data were plotted for the individual lesions at pre and post-treatment, respectively. (b) For the group of sham and WBRT, mean tumor ADCs at pre ($n = 59$ vs. 44) and post-treatment ($n = 90$ vs. 65) were plotted. The post-treatment mean ADC ($0.83 \times 10^{-3} \pm 0.01$ mm^2/s) was significantly higher than the pre-treatment value ($0.75 \times 10^{-3} \pm 0.02$ mm^2/s; $p < .05$) in the WBRT group, while there was no significant difference between pre and post-treatment in the sham group ($0.76 \times 10^{-3} \pm 0.01$ mm^2/s vs. $0.75 \times 10^{-3} \pm 0.02$ mm^2/s). Mean ± SE, *$p < .05$.

Author Manuscript Author Manuscript Author Manuscript Author Manuscript

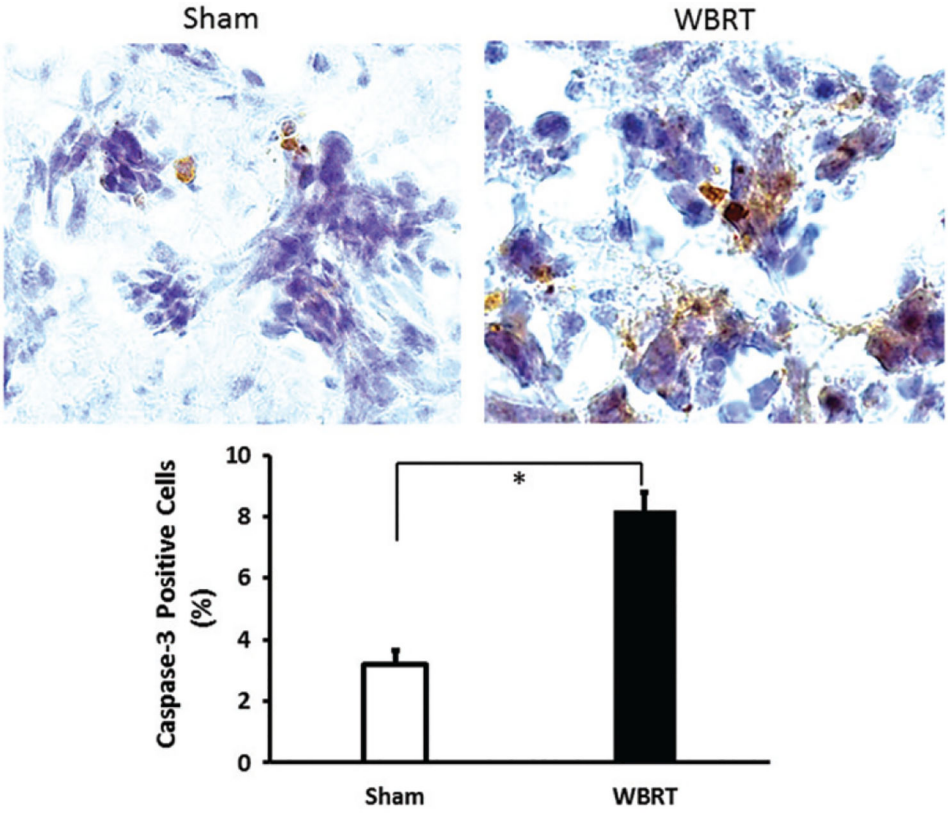

Figure 3.

Caspase 3 immunostaining of WBRT induced apoptosis. Immediately after the post-treatment MRI scans, brain metastases-bearing mice were sacrificed and brains were dissected. Frozen sections were prepared and immunostained with anti-caspase 3 antibody. Positively stained apoptotic tumor cells were presented in the representative sham and WBRT treated tumor. Quantitative analysis of a group of sham ($n = 3$) and WBRT ($n = 3$) indicated significantly more apoptotic cells in the WBRT tumors (mean = 8.8 ± 0.6%) than the sham tumors (3.2 ± 0.4%; $p < .05$). Mean ± SD.

Author Manuscript Author Manuscript Author Manuscript Author Manuscript

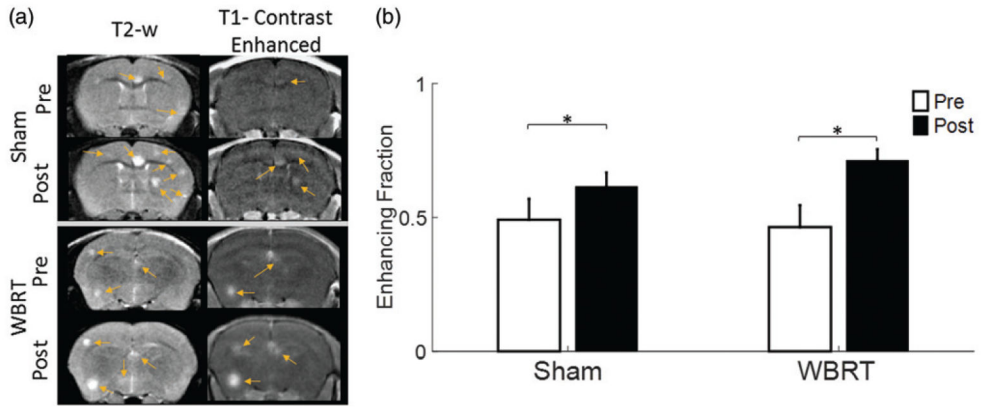

Figure 4.

T1-weighted contrast enhancement indicating disrupted BBB. (a) Representative T2-w and T1-w contrast-enhanced images of a WBRT and sham-treated mouse brain were obtained at pre and post-treatment. Many of the hyperintense lesions on T2-w images were not enhanced on T1-w contrast images, indicating heterogeneous BBB permeability among individual lesions. (b) Fractions of tumors with T1 contrast enhancement at pre and post-treatment were plotted. Significant increase in enhancing fractions was found at post-treatment in both the sham (0.62 ± 0.05 vs. 0.49 ± 0.08) and the WBRT (0.71 ± 0.04 vs. 0.46 ± 0.08) group. Mean ± SE, *$p < .05$.

Author Manuscript Author Manuscript Author Manuscript Author Manuscript

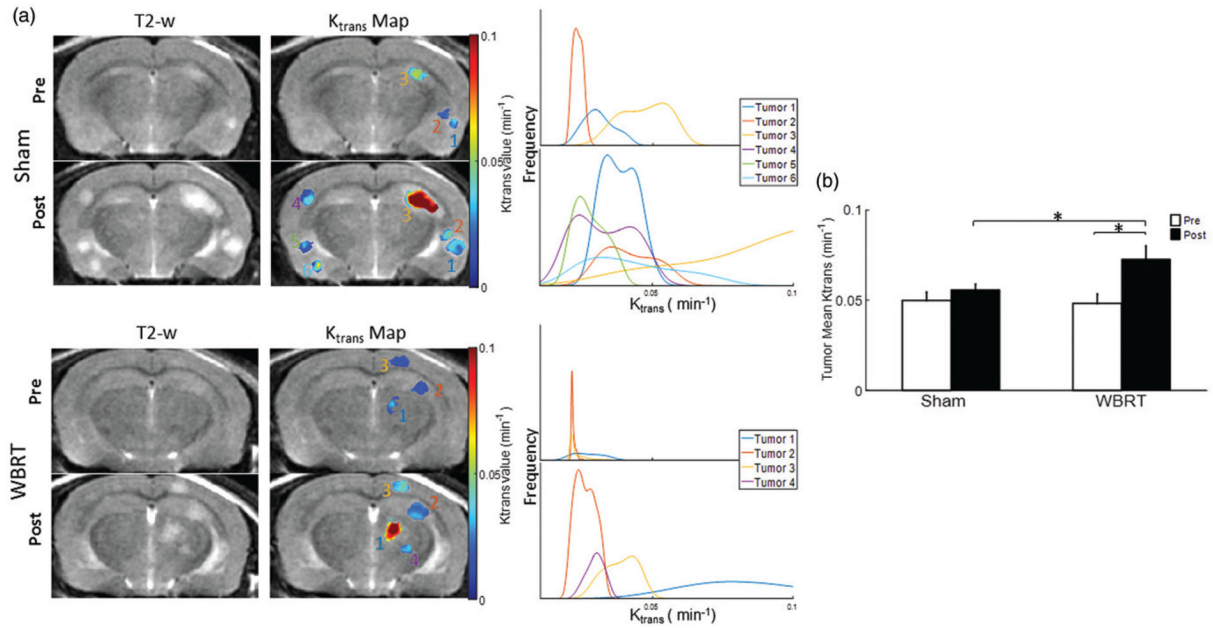

Figure 5.

DCE MRI of BTB permeability. (a) Quantitative vascular permeability K_{trans} maps from DCE MRI were generated for the same brain lesions as shown in Figure 3 and overlaid on T2-w images. Histogram plots of voxel by voxel K_{trans} data revealed inter- and intratumoral heterogeneity in BTB permeability. (b) Mean K_{trans} were obtained for the pre and post-treated brain lesions in the sham and WBRT group. Significant increase in mean K_{trans} was found at post-treatment in the WBRT tumors (0.073 ± 0.007 vs. 0.048 ± 0.005 min^{-1}). Compared to the sham treatment (mean = 0.056 ± 0.003 min^{-1}), the WBRT tumors had a significantly higher K_{trans}. Mean ± SE, $*p < .05$.

Author Manuscript Author Manuscript Author Manuscript Author Manuscript

Table 1.

Quantification of tumor size, new tumor incidence, ADC, K_{trans}, and tumor-enhancing fraction.

						ADC ($\times 10^{-3}$ mm^2/sec)		
		Tumors per Animal	**Tumor Size (mm^3)**	**New Tumors (%)**	**Enhancing Fraction**	**Tumor**	**Contralateral**	**K_{trans} (min^{-1})**
Sham	Pre	16.8 ±9.4	0.28 ±0.22		0.49±0.08	0.75 ± 0.01	0.65 ±0.06	0.050± 0.005
	Post	22.8 ± 11.8	0.44 ±0.31 **	41.5 ±29.2	0.62 ±0.05 *	0.77 ± 0.02	0.64±0.09	0.056± 0.003
WBRT	Pre	17.4 ±11.7	0.23 ±0.12		0.46±0.08	0.75 ± 0.02	0.64±0.05	0.048± 0.005
	Post	20.4 ± 13.2	0.34 ± 0.21 **,#	20.7 ±16.1	0.71 ±0.04 *	0.83 ±0.02 *,#	0.65 ±0.07	0.073 ± 0.007 *,#

* $p < .05$.

** $p < .01$ compared to pre-treatment.

\# $p < .05$ compared to sham group post-treatment.